

See discussions, stats, and author profiles for this publication at: <https://www.researchgate.net/publication/233781906>

# Spectroscopy and Imaging of Plasmonic Modes Over a Single Decahedron Gold Nanoparticle: A Combined Experimental and Numerical Study

ARTICLE *in* THE JOURNAL OF PHYSICAL CHEMISTRY C · NOVEMBER 2012

Impact Factor: 4.77 · DOI: 10.1021/jp3103782

---

CITATIONS

11

---

READS

58

2 AUTHORS, INCLUDING:



Tapas Kumar Chini

Saha Institute of Nuclear Physics

68 PUBLICATIONS 681 CITATIONS

SEE PROFILE

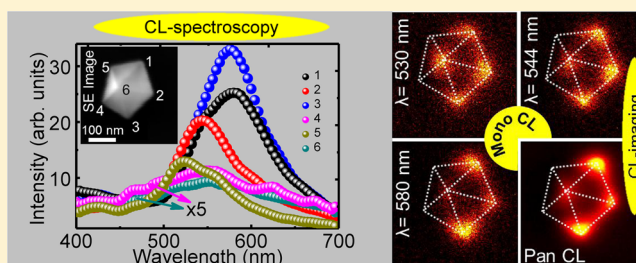
# Spectroscopy and Imaging of Plasmonic Modes Over a Single Decahedron Gold Nanoparticle: A Combined Experimental and Numerical Study

Pabitra Das and Tapas Kumar Chini\*

Surface Physics Division, Saha Institute of Nuclear Physics, 1/AF Bidhannagar, Kolkata 700 064, India

**S** Supporting Information

**ABSTRACT:** Employing cathodoluminescence (CL) spectroscopy and imaging in a field emission gun (FEG) scanning electron microscope (SEM), we study localized surface plasmon (LSP) modes on individual tilted gold nanodecahedron sitting on a silicon substrate. We experimentally resolve three distinct LSP modes in the far-field radiation acquired via CL. The experimental spectra and intensity maps of plasmon modes are in excellent agreement with the spectra and 2D-CL image obtained from finite difference time domain (FDTD) simulations. Detail analysis reveals the signature of a quadrupolar surface plasmon mode in addition to the two dipolar modes along azimuthal and polar direction of the decahedron. The experimental method and the theoretical formalism presented here provide useful insight into the plasmonic behavior of complex shaped metal nanoparticle supported by a high index substrate.



## INTRODUCTION

The optical response of noble metal nanoparticles (MNPs) is governed mainly by the concept of the collective oscillation of conduction electrons in MNP, known as localized surface plasmon (LSP) or particle plasmon. LSP when excited<sup>1–3</sup> resonantly with a particular wavelength of the exciting light or evanescent wave associated with fast-moving electrons, can lead to strong light absorption and scattering. Another striking feature of the LSP resonance is the considerable localized enhancement of the near-field amplitude at the nanostructured metal surface allowing electromagnetic (EM) energy to be confined at the subwavelength length scale and similar enhancement of the far-field radiation intensity. These enhanced EM fields have several interesting effects, such as enhanced fluorescence,<sup>4</sup> enhanced photocarrier generation,<sup>5</sup> and surface enhanced Raman scattering (SERS),<sup>6</sup> that can have potential applications in biosensing, photovoltaics, and single molecule detection. Often the local EM field enhancement in the plasmonic structures is confined spatially on length scales of ~10–50 nm and varies strongly with the morphology and composition of nanoparticles. Consequently, investigation of the electromagnetic field distribution associated with nanoparticle SPs (more specifically, LSPs) requires an experimental probe not only of sufficient spectral resolution but also of sufficient degree of spatial resolution for deeper understanding of light-matter interaction at the nanometer length scale.<sup>7–10</sup>

Mapping the spatial variation of the photon emission<sup>11–16</sup> is a direct probe of resonant modes of plasmonic nanostructures and, consequently, provides a direct way to map the local electric fields. Due to the simplicity of the instrumental setup, a large body of the MNP optical studies have been performed

using optical dark-field microscopy (DFM),<sup>17–20</sup> which provides excellent spectral resolution. However, DFM is constrained by the diffraction limit to a spatial resolution of about half a wavelength and, consequently, it cannot be used to image the spatial profile of the plasmon resonances on length scales below ~200 nm. Near-field scanning optical microscopy (NSOM),<sup>14</sup> on the other hand, can achieve a resolution of ~20 nm or slightly better but (in the case of NSOM) is constrained by the requirement of fabricating very sharp tips, and furthermore, interaction of the tip with light in the structure often perturbs the LSP mode,<sup>22</sup> making it challenging to probe the detailed spatial profile of the resonance. So, the search for a nonperturbing probe to directly image the plasmonic local field with high spatial resolution remains a challenging task. Alternatively, electron beam based tools,<sup>3</sup> such as cathodoluminescence (CL) spectroscopy and imaging<sup>11–13,15,16</sup> through the detection of emitted photons in a scanning/transmission electron microscope (SEM/TEM) or electron energy loss spectroscopy (EELS)<sup>23–25</sup> through the detection of energy loss suffered by the inelastically scattered transmitted electrons in a TEM, are shown to constitute an excellent probe of plasmons that allows capturing even subnanometer resolution information in the spatial domain. Although EELS has been shown as the best single particle spectroscopy technique to probe plasmons on a MNP with unmatched spatial and spectral resolution,<sup>9,25</sup> it suffers from the drawback that samples must be electron transparent (typically below 100 nm), which

**Received:** October 19, 2012

**Revised:** November 12, 2012

**Published:** November 20, 2012



prevents it from being used in case of thick samples sitting on a substrate. On the other hand, CL in a SEM does not suffer from such limitations and can be used as a potential tool for obtaining correlated single particle spectroscopic and microscopic information from the same region of interest including the substrate effect, a unique feature not easily accessible in EELS.

Decahedron or pentagonal bipyramid shaped nanostructure of Au has drawn considerable attention recently due to their application as biosensors, which can be realized by exploiting their inherent optical anisotropy and highly localized plasmon modes.<sup>20,21,25,26</sup> The interest in this direction has also been driven by the theoretically demanding nature of predicting far-field scattering and extinction of nonspherical morphologies using the electrodynamics based computational tools, such as the finite difference time domain method (FDTD)<sup>27,28</sup> and the boundary element method (BEM).<sup>20,25</sup> Although a rigorous electromagnetic calculations based BEM numerical approach can nicely predict the CL spectrum and CL mapping on Au decahedron as reported quite recently,<sup>25</sup> experimental realization of site specific spectroscopy and imaging of LSP modes over the Au decahedron could not be achieved using the CL-SEM technique due to the comparable size ( $\sim 58$  nm) of the particle and the diameter of the e-beam probe employed in a conventional LaB<sub>6</sub> source SEM in the reported study.<sup>25</sup>

Here, employing the CL in a field emission gun (FEG) SEM, we have demonstrated the mapping of the spatial variation of SP assisted photon emission in the visible range at the pentagonal base corners and apex of a  $\sim 40^\circ$  inclined gold decahedron with edge length of  $\sim 110$  nm after recording the emission spectra at different locations of the nanoparticle. This is the first experimental demonstration of site specific spectroscopy and imaging of two dipole-active SP modes along the azimuthal and polar direction in addition to a distinct quadrupolar SP modes on an isolated gold decahedron using CL-SEM technique where the results are well interpreted on the solid background of detail FDTD based numerical modeling. Although the FDTD method has been employed by others,<sup>15</sup> the FDTD approach to construct a 2D-CL image used here is relatively new and has been reported by us quite recently.<sup>16</sup> The approach and methodology presented here could be used to investigate the complex nature of plasmonic modes of nanoparticles having various asymmetric geometries. The CL-SEM technique applied here is based on the fact that energy is coupled from incident energetic electrons to the local plasmonic modes of the metal nanostructure and subsequently to propagating light modes that constitute one of the prominent decay channels for the plasmons. Consequently, the CL emission map gives the information about the EM local density of states (LDOS)<sup>29–31</sup> with high spatial resolution. LDOS in turn is related to the local electric field intensity at a particular wavelength at a fixed point and it reflects the local EM field enhancement in a metallic nanostructure.

## ■ EXPERIMENTAL SECTION

**Material Synthesis.** Gold decahedra in the present work are synthesized by a seed mediated growth method, which is a small variant of the protocol used by Wu et al.<sup>32</sup> and described in our recent work.<sup>16</sup> Before doing any microscopy or CL study, the colloidal Au solution was diluted sufficiently with deionized water. The diluted solution was then carefully dispersed on a Si(100) substrate by dropcasting and desiccation and dried under ambient condition for 2 days, and after that,

the nanoparticle containing specimen was inserted into the SEM chamber. This chemical synthetic approach produces a mixture of nanospheres, triangular prisms, decahedra, and faceted rods of different sizes. Among the randomly distributed nanoparticles, a single nano decahedron was selected for study.

**CL Measurements.** CL or electron beam induced radiation emission (EIRE) imaging/mapping on an isolated single decahedral Au nanoparticle was performed in a ZEISS SUPRA40 SEM equipped with the Gatan MonoCL3 cathodoluminescence system, the details of which have been described elsewhere.<sup>33</sup> The ZEISS SUPRA40 SEM has a hot Schottky field-emission gun (FEG) and the attached MonoCL3 system uses a retractable paraboloidal light collection mirror. The parabolic mirror collects light that is emitted from the sample covering  $1.42\pi$  sr of the full  $2\pi$  of the upper-half sphere and collimates it through a hollow aluminum tube to a 300 mm Czerny–Turner type optical monochromator, and finally the signal is fed to a high-sensitivity photomultiplier tube (HSPMT). In the present study, data were recorded with an electron acceleration voltage of 30 kV and beam current of about 15 nA with a beam diameter of  $\sim 5$  nm. The electron beam was directed onto the sample surface through a 1 mm diameter opening in the mirror. To ensure maximum efficiency of light collection, the top surface of the sample is kept at the focal plane of the mirror, which lies approximately 1 mm below the bottom plane of the mirror. Before every set of experiment we adjusted this optical focal plane with utmost care using the stepper motor controlled sample stage. The CL system in conjunction with the SEM can be operated in two modes, namely, monochromatic (mono) and panchromatic (pan). In the monochromatic mode of CL operation, the focused e-beam is either scanned over the sample or positioned on a desired spot while the emitted light from the sample passing through the monochromator allows the emission spectra to be recorded serially in the range 400–700 nm for the HSPMT used in the present case. The spectral step of 4 nm and a dwell time of 0.25 s for a band-pass of  $\sim 11$  nm were maintained while collecting the CL spectra in the present experiment. Following the collection of spectra, the monochromatic photon map is built up at a selected peak wavelength of the EIRE spectrum by scanning the e-beam over the sample. Note that bright pixels in the mono CL image are due to an e-beam position that strongly excites a resonant plasmonic mode, whereas the photons emitted and subsequently collected may come from anywhere over the MNP once a mode has been excited. Therefore, the image contrast in CL is a measure of the ability of the e-beam to locally excite the modes. In the panchromatic mode of CL operation, on the other hand, the emitted light skips the monochromator and all of the light is carried to the detection optics and all the wavelengths emitted from the sample contribute to the resulting panchromatic photon map. The contrast of the pan-CL image is determined by the variation of the integrated photon counts at each pixel in the sensitivity range of the HSPMT detector. To correct the spectrum for substrate effect, we took the separate spectrum from the silicon substrate at a position  $\sim 1$   $\mu\text{m}$  away from the MNP. All the spectra presented in this article are corrected with respect to the substrate. All the experimentally acquired images are of  $(200 \times 200)$  pixels and each pixel corresponds to a length of 1.7 nm. The typical acquisition time for one frame of  $(200 \times 200)$  pixels is 20s.

**FDTD Simulation for Electron Beam Excitation.** Detail analysis of the experimental data on the surface plasmon

assisted photon emission from MNPs requires solutions of Maxwell equations for the geometry of the MNP under consideration. However, analytical solutions exist<sup>3</sup> only for simple geometries, like the sphere or the infinite cylinder. For the decahedral Au nanoparticle considered here, we have performed 3D-FDTD numerical simulations. In FDTD, the macroscopic Maxwell's equations are solved in discretized space and discretized time to follow the response of a material to any applied EM field. We have used here a commercially available FDTD code (from Lumerical Solutions, Canada). For numerical investigation of the e-beam excited photon emission in a CL setup, the e-beam can be modeled as a line current density source represented as

$$J(t, \vec{r}) = -ev\hat{u}_z\delta(z-vt)\delta(x-x_0)\delta(y-y_0) \quad (1)$$

where  $e$  is the electronic charge,  $v$  is the velocity of electron,  $(x_0, y_0)$  represents the position of the electron beam,  $z$  is the direction of electron velocity, and  $\hat{u}_z$  is the unit vector along  $z$  direction. In the simulation, this current density is modeled as a series of dipoles with temporal phase delay  $(z/v)$  that is related to the electron velocity,  $v$  (here  $v = 0.32c$ , corresponding to the 30 keV electron energy used in the present experiment and  $c$  being the velocity of light in free space).

To simulate the emission spectra, the radiative energy component of the induced electromagnetic field is calculated by integrating the Poynting vector normal to an arbitrary large surface in the upper  $z$  half-plane for wavelength ranging from 400 to 700 nm. Our method of obtaining the simulated radiation intensity maps mimics the equivalent raster scanning situation of the e-beam as done for CL mapping in the actual experiment. A more detailed description of the CL spectroscopy and imaging using FDTD can be found in our recent work.<sup>16</sup>

As a time domain technique, a single simulation can be used to provide simulation results at many frequency points. This provides the ability to analyze and optimize the design across a wide wavelength range, but this is only true to the extent that the models used to describe the dispersive nature of the constituent materials are themselves accurate over the wavelength range of interest. To overcome the multiwavelength challenge, we have used Lumerical's multicoefficient materials (MCMs). MCMs rely on a more extensive set of basis functions to better fit dispersion profiles that are not easily described by Drude, Debye, and Lorentz materials. With a comparable cost in model complexity and computation speed, the resulting MCM model is superior to the Lorentz–Drude model. The dielectric constant/refractive index used in the calculations are obtained from generalized MCM that fits the experimental dispersion data obtained from *CRC Handbook of Chemistry and Physics*.<sup>34</sup> The thickness of the Si substrate in the simulation has been assumed to be 4  $\mu\text{m}$  with a fixed refractive index of 4 (nondispersive) in the wavelength range 400–700 nm. We used a constant dielectric material for simplicity but have compared results with simulations (see Figure SI.1 of Supporting Information) using a dispersive Si substrate and found no significant differences. Moreover, a dispersive substrate makes the simulation slower and consumes more memory compared to that for a nondispersive substrate. As the EM field can diverge near sharp corners separating two continuous media, we introduce roundness with a radius of curvature of 5 nm in the decahedra corners and in both the apexes, which is consistent with the morphology obtained from the SEM image. In actual physical systems also, an absolutely

sharp corner is not possible as atomic distances impose a restriction.

## RESULTS AND DISCUSSION

**CL Spectroscopy and Imaging.** In Figure 1a, CL spectra taken from different corners of the pentagonal base (marked as

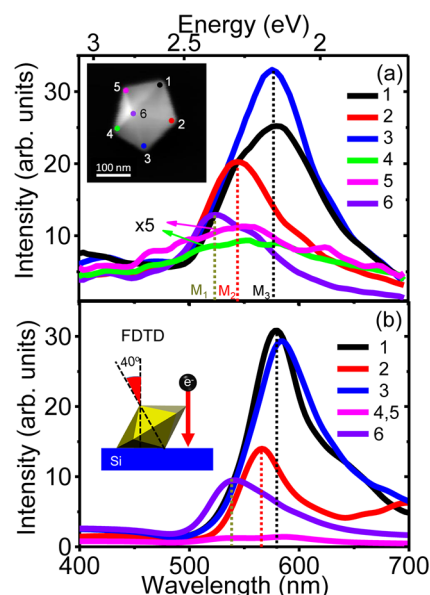


**Figure 1.** Site specific CL spectroscopy from gold decahedron of side edge length 110 nm. (a) Experimental CL spectra for different e-beam positions marked as 1–6. The inset shows the SE image with the e-beam impact position marked by color spots. The e-beam energy is 30 keV. Only corner positions 1, 2, and 3 and the center position 6 show detectable luminescence above noise level. For better visual representation the spectra from corners 4 and 5 have been multiplied by a factor of 5 and then plotted. Spectral peaks at 530, 544, and 580 nm are observed. We mark the corresponding modes as  $M_1$ ,  $M_2$ , and  $M_3$ , respectively. (b) The FDTD simulated CL spectra for different position of e-beam impact (schematic shown in the inset of (b)). Spectral peaks at 540, 563, and 580 nm are observed. The geometry that we simulated is the same as obtained from SEM image; i.e., the decahedron is tilted with one of its face touching the substrate, the tilt angle being 40°.

1, 2, ..., 5) and the apex (marked as 6) of the decahedron is shown (inset: SE image of the decahedron). The decahedron is inclined with respect to the surface normal by an angle  $\sim 40^\circ$ . From the SE image, the decahedron side edge length ( $L$ ) is found out to be  $\sim 110$  nm. By recording the SE image at a high tilt angle ( $50^\circ$ ) of the sample stage and after necessary tilt correction in SEM, we measured the distance between two central tips (apexes) of the decahedron to be  $\sim 120$  nm. The geometrical height  $h$  (distance from the center of the pentagonal base to the central tip) of a decahedron in term of its' side edge length ( $L$ ) is given by the formula<sup>26</sup>

$$h = \frac{1}{10} \sqrt{50 - 10\sqrt{5}} L \quad (3)$$

and the calculated  $h$  turns out to be  $\sim 58$  nm, yielding the distance between the apexes to be  $\sim 116$  nm which agrees well with the value 120 nm obtained from the SE image as mentioned above. This also shows that the measured aspect ratio of the decahedral particle under study is consistent with the geometrical relationship for a regular pentagonal bipyramid.



The height obtained from the geometrical formula has been used in all our simulations. Experimental CL spectra of Figure 1a depict that the spectral peak intensity and peak position is highly dependent upon the point of excitation of e-beam over the nanoparticle. In Figure 1b, we show that the FDTD simulated CL spectra matches extremely well with the experimental one. The highest spectral peak intensity at wavelength 580 nm is observed when the e-beam is focused near the corner marked 3 of the decahedron. For e-beam impact near corners 4 and 5, which are close to the Si substrate, the radiated intensity is about 15 times smaller than the highest intensity obtained at point 3. The decahedron in our experiment is supported on the substrate with one of their faces in contact with it, and consequently, that face has a strong interaction with the high index substrate like Si (used in the present case). The localized surface plasmon resonance (LSPR) will tend to radiate mostly into the high index substrate,<sup>35</sup> resulting a reduction in the amount of emitted light at the upper hemisphere and this is the reason behind negligible emission intensity for e-beam excitation at corners 4 and 5. The size dependent optical properties of Au decahedra show two separate dipolar modes, namely azimuthal and polar, which arise due to the inherent anisotropy of the decahedral geometry.<sup>20,21,25</sup> For the decahedral particle, the azimuthal mode is associated with the oscillation of charges of opposite polarity ( $\pm$ ) in the plane of the pentagonal base (or the equatorial plane) of the particle whereas the polar mode corresponds to the oscillation of charges along the 5-fold symmetry axis of the decahedron.

The resonance condition of the polar mode is achieved at a lower wavelength (higher energy) compared to the azimuthal one. With an increase in the particle size, these two modes (namely, dipolar azimuthal and polar modes) red shift and get broadened. For decahedra of side edge length >60 nm, multipolar modes higher than the dipolar one, i.e., quadrupolar mode, begin to develop<sup>20</sup> with an energy intermediate between the azimuthal and the polar dipole modes. The origin of the higher order modes is linked with the retardation of the electromagnetic signal as it propagates along the extension of the particle. Consequently, quadrupolar mode is more pronounced for larger particles where efficient coupling to external light is easily attained via larger polarizability. Higher order modes are also expected to be more sensitive to the breaking of decahedral axial symmetry.<sup>21</sup> Hence we can expect the presence of a quadrupolar mode other than the dipolar one for the decahedron with side edge length 110 nm used in the current study.

The major peak as found in our experiment for e-beam focused at points 1 and 3 corresponds to the azimuthal dipole mode of plasmon oscillation, which we confirmed using FDTD simulations (to be discussed later). In the experimental spectra, intensity of the major peak at  $\sim 580$  nm for e-beam excitation at corner 3 is 1.3 times larger than that of corner 1 even though these two corners are equivalent in the  $40^\circ$  tilted geometry, which is reflected in the simulated CL spectra from corners 1 and 3 (Figure 1b). We also identified a weak polar mode peaked at  $\lambda = 530$  nm for e-beam excitation at the apex (marked as 6). The polar mode peak intensity is 2.75 times lower than the maximum intensity for the azimuthal mode. A slightly blue-shifted peak (compared to the 580 nm for excitation at corner 1 or 3) is obtained at 544 nm while the electron probe is focused near corner 2. The maximum intensity for excitation at corner 2 is  $\sim 1.6$  times less than that of

corner 3. In the FDTD simulation, we find the same peak at 563 nm (Figure 1b) and assigned it to the quadrupolar mode (discussed later in this section). For convenience, in the rest of the paper we will refer to the modes associated with the spectral peaks 530, 544/563, and 580 nm as  $M_1$ ,  $M_2$ , and  $M_3$ , respectively. A summary of the modal peak positions and the corresponding fwhm values is given in Table 1. The major

**Table 1. Experimental and Simulated CL Spectral Peak Positions Corresponding to Assigned Modes**

		mode assignment		
		$M_1$	$M_2$	$M_3$
experimental	peak position (nm)	530	544	580
	fwhm (nm)	70	67	82
simulated	peak position (nm)	540	563	584
	fwhm (nm)	43	47	58

modes were fitted with a single Gaussian in the wavelength range 500–650 nm in all the cases except the simulated  $M_1$  mode where the best fit was obtained with two Gaussians, one at 540 nm (fwhm 43 nm) and another one at 580 nm (fwhm 59 nm). In Figure 2b–e, experimental CL maps and, in Figure

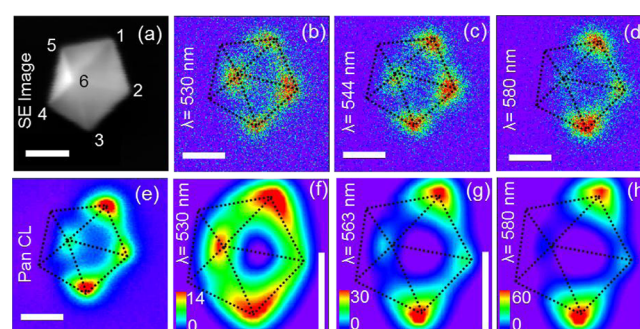


**Figure 2.** CL imaging on an isolated gold decahedron on silicon. (a) SE image of the decahedron of side edge length 110 nm. It is tilted with respect to the surface normal by an angle  $\sim 40^\circ$ . (b)–(d) Monochromatic CL emission maps recorded at wavelengths 530, 544, and 580 nm, respectively. (e) Panchromatic CL emission map obtained by collecting photons at all wavelengths. All the images (b)–(e) are acquired in  $200 \times 200$  pixels, and the total exposure time in recording one frame is 20 s. (f)–(h) FDTD simulated 2D-CL emission maps at wavelengths 530, 563, and 580 nm, respectively. The scale bar in all the images is 100 nm.

2f–h, the FDTD simulated CL images have been shown for different spectral peak wavelengths. Because the spectral distance between modes  $M_3$  and  $M_1$  or  $M_2$  is smaller than the plasmon broadening, the CL map of the weaker polar mode  $M_1$  picks up intensity from modes  $M_2$  or  $M_3$  or both the modes, which is reflected in the experimental and simulated monochromatic CL images (Figure 2b,f). So the polar mode is hidden in the tails of modes  $M_2$  and  $M_3$ . In conventional single particle spectroscopy techniques, like dark field microscopy (DFM), where the whole particle is illuminated, this mode cannot be obtained experimentally unless the particle is oriented with respect to the substrate in such a way that the overall contribution of the polar dipole mode is comparable or larger than the azimuthal dipole mode at the polar mode wavelength. Moreover, more absorption than scattering along the polar direction adds difficulty to the detection of the polar mode. However, this situation is circumvented by the use of e-

beam spectroscopy based techniques, like EELS or CL where a finely focused (nm size) e-beam can pinpoint the desired location of the MNP and excite such hidden modes. One can notice a mismatch of 19 nm in spectral peak position between the experimental (544 nm) and simulated (563 nm) spectra when the electron probe is focused near corner 2 of the decahedron, which can be explained as follows: Experimentally we take the spectra in serial mode by allowing one wavelength at a time to pass to the HSPMT through a sharp knife edge slit with an opening of 4 nm. This introduces a spectral band-pass of  $\sim 11$  nm. This band-pass can cause the shift between experimental and simulated spectra. There could be other reasons also, such as the uncertainty in the exact shape of the decahedron obtained from SEM imaging (on the basis of which we modeled the structure), the uncertainty in the exact location of the e-beam due to small drift of the specimen during spectrum acquisition, and the possibility of the presence of CTAB surfactant layer between the particle and the substrate causing a change of dielectric environment not considered in the simulation. Apart from the monochromatic and panchromatic CL image, the SE image is also acquired simultaneously (Figure 2a). This allows us to directly correlate the CL spectroscopic signal and photon maps with the nanoparticle morphology. The spatial variation of emission that we see in the monochromatic CL images is a direct probe<sup>11,12</sup> of resonant modes of MNP. Spatial variation of the CL emission is caused when the field produced by the e-beam couples strongly to the EM eigenmodes of the structure. The coupling is strongest when the e-beam is located near the largest EM fields of the resonant SP eigenmodes and when the modal fields have proper polarization to couple to the polarization of the vertical e-beam.

**Effect of Tilt Angle on the Plasmon Modes.** FDTD simulation helps us to extend our study further to understand the decahedron tilt angle dependence of the plasmon modes and their relative intensity, which in turn can explain the physical origin of the modes that we observe experimentally. We have studied the effect of variation in tilt angle,  $\theta$  from  $0^\circ$  to  $40^\circ$  on the relative intensity of various modes. This effect is monitored for e-beam excitation at corner 2. The plots in Figure 3 show one prominent peak occurring at  $\sim 610$  nm wavelength and a relatively less prominent peak at  $\sim 563$  nm is also overlaid in the spectra for tilt angle  $\theta = 0^\circ$ . The 610 nm peak is obtained for corner excitation and is the most intense one, and it is identified as  $M_3$ , which blue shifts to 580 nm when  $\theta$  increases to  $40^\circ$ . For excitation at corner 2, the 563 nm peak becomes prominent and is most efficiently excited for  $\theta = 40^\circ$ . Now let us recall here that a tilt angle of  $40^\circ$  is our experimental configuration. We got an experimental peak at  $\sim 544$  nm (spectrum 2 of Figure 1a) and a simulated one at 563 nm (spectrum 2 of Figure 1b) and named it as  $M_2$ . So, the less prominent peak at  $\sim 563$  nm for  $\theta = 0^\circ$  is the same as  $M_2$ . Things become quite complicated as well as interesting when the decahedron tilt angle is nonzero. Mode  $M_2$ , which was less prominent in  $\theta = 0^\circ$  becomes dominant for  $\theta = 40^\circ$ . In the intermediate orientations (between  $0^\circ$  and  $40^\circ$ ) of the MNP, with increasing  $\theta$  the intensity of  $M_3$  decreases. Apart from this, a new peak begin to appear from  $\theta = 20^\circ$  at wavelength greater than 580 nm, which red shifts with increasing  $\theta$ . The origin and the cause of red shift of this peak are not clear to us at this moment. At  $\theta = 20^\circ$ ,  $M_2$  mode intensity is almost same as with  $M_3$  and finally at  $\theta = 40^\circ$ , the only detectable mode in the 400–700 nm wavelength range is  $M_2$ .

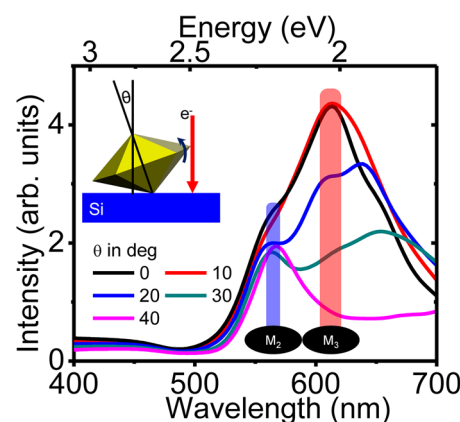


**Figure 3.** FDTD simulated CL spectra for e-beam excitation at corner 2 for different orientation of the decahedron with respect to the substrate normal. We have shown change in the spectra for variation in the tilt angle from  $0^\circ$  to  $40^\circ$  (beyond  $40^\circ$  is not allowed in reality due to the restriction of the substrate). By tilt angle ( $\theta$ ), we mean the angle between the substrate normal and the line joining the two apexes of the decahedron. The shaded regions include the variations of peak position of modes  $M_2$  and  $M_3$ . The FDTD mesh size used in this particular simulation was  $(1 \text{ nm} \times 1 \text{ nm} \times 1 \text{ nm})$ .

Now, regarding the excitation at corners 1 and 3 (Figure 1a,b), the  $M_3$  mode shows a blue shift from 610 to 580 nm when the tilting configuration is changed from  $0^\circ$  to  $40^\circ$ . When the tilt angle is  $0^\circ$ , all the corners (marked as 1, ..., 5) are symmetric ( $C_{5v}$  symmetry<sup>25</sup>) and equivalent. As  $\theta$  increases from  $0^\circ$  to  $40^\circ$ , corners 1 and 3 remain equivalent with respect to the vertical distance from the substrate. However, corner 2 is elevated more from the substrate with increasing  $\theta$ . From the FDTD 3D simulation layout, we calculate the vertical distance of corner 1 or 3 and 2 from the top surface of the substrate to be  $\sim 66$  and  $108$  nm for  $\theta = 40^\circ$ . The spectral changes that we see with increasing tilt angle seems to be linked with the change of distance of decahedron corners with respect to the substrate, meaning the proximity of the substrate with respect to the point of excitation.

The interaction of a nanoparticle with the substrate on which it is sitting can affect the LSPR dramatically.<sup>36</sup> Due to the emission going into the high index substrate and not reaching the CL detector as we already discussed, we could not reproduce the shift of the mode in contact with the substrate (corners 4 and 5) as found in ref 25. This local shift is quite disputed even in the case of relatively more simple systems like nanocubes for which the main dipolar mode split due to the substrate,<sup>37</sup> which has been directly observed in EELS.<sup>38</sup> For a structure quite complicated as the decahedra, the effect of the substrate is not trivial. For silver nanocubes quadrupolar resonance peak is associated with large field away from the substrate and a dipolar peak is associated with large field near the substrate. The former is mentioned as “distal” mode and the later is mentioned as “proximal” mode in ref 37. In the present study, the mode associated with excitation at corner 2 (distance from substrate  $\sim 108$  nm) and the mode associated with excitation at corner 1 or 3 (distance from substrate  $\sim 66$ ) is consistent with the existence of such a “distal” and “proximal” mode hypothesis by Ringe et al.<sup>37</sup> With increasing  $\theta$  for excitation at corner 1 or 3,  $M_3$  sustains (peak position blue shifts by about 30 nm from 610 to 580 nm) and  $M_2$  diminishes whereas, for the same excitation at corner 2,  $M_3$  gradually decreases and  $M_2$  becomes dominant. So, for a decahedral

particle sitting on a substrate, variation of tilt angle basically manifests the effect of substrate on the LSP modes of the particle more prominently than the role of tilted configuration itself.

**Assignment of Luminescence Peaks.** To gain further insight into the possible modes of LSP oscillations supported by the gold decahedron structure, we have plotted in Figure 4b,c the simulated vectorial distribution of the electric field ( $\vec{E}$ )

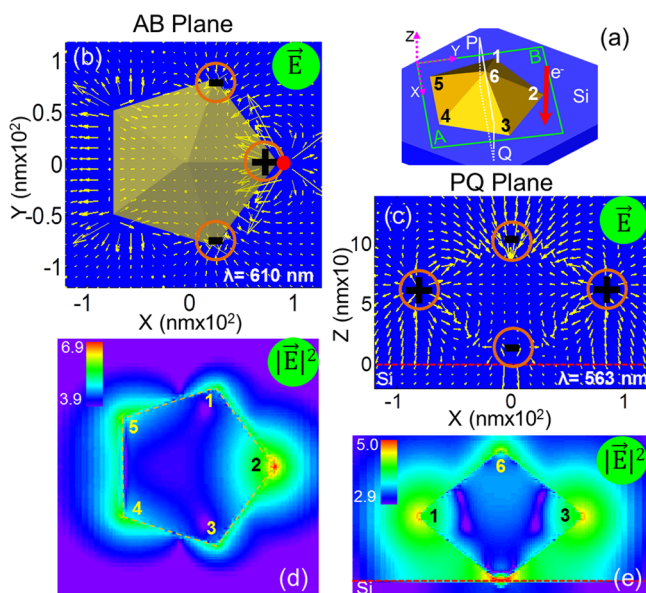


**Figure 4.** (a) Schematic of the simulated decahedron of edge length 110 nm sitting vertically on Si. The simulated vectorial distribution of the electric field ( $E$ ) and the  $E$  intensity ( $|E|^2$ ) has been calculated from two planes, namely AB and PQ, as shown. The AB plane is parallel to the XY plane passing through the equatorial region of the decahedron and perpendicular to the 5-fold symmetry axis. The PQ plane is a parallel to the XZ plane containing the 5-fold symmetry axis covering the particle height and extending some distance into the substrate. The red arrow indicates the position of the e-beam impact. (b), (c) Vector plots of the electric field ( $E$ ) from AB (showing dipole mode along the edge length at 610 nm) and the PQ plane (showing quadrupole mode at 563 nm), respectively. (d), (e) Calculated near-field intensity maps at planes AB and PQ, respectively. The field intensity has been plotted in log scale. The red circular spots in the images indicate the point of e-beam impact.

in the planes AB and PQ passing through the pentagonal base and polar axis of the Au decahedron as shown in Figure 4a for the most simple case of  $\theta = 0^\circ$  where the point of e-beam excitation is located near one of the corners (corner 2 in the figure). Simulated CL spectra of Figure 3 show that at  $0^\circ$  both  $M_2$  and  $M_3$  modes are present. The simulated vector maps of Figure 4b reveals that the major mode  $M_3$  supported at the resonant wavelength of 610 nm is the azimuthal dipolar mode where charges with opposite polarity ( $\pm$ ) could be accommodated at two nearby corners like 1–2 or 2–3 etc. On the other hand, for the resonant wavelength at 563 nm, the vector map of the electric field (Figure 4c) shows that the mode  $M_2$  is quadrupolar in nature. The induced near-field electric intensity ( $|E|^2$ ) maps at 610 and 563 nm is shown in Figure 4d,e. Azimuthal dipolar mode  $M_3$  shows large field enhancement at the pentagonal base corners and edges. The quadrupole mode  $M_2$ , on the other hand, exhibits the near-field enhancements at the corners as well as the apexes, although their relative

intensity is different, as shown in the colored intensity scale bar. The experimental verification of spectral signature of a quadrupolar mode on a gold nanodecahedra of similar dimensions as employed in the present study has been reported earlier<sup>20</sup> by DFM technique. And it is also well studied that the relative intensity of the quadrupolar and azimuthal dipolar mode depends highly on the particle orientation with respect to the substrate. But in DFM the whole particle is illuminated and, consequently, the contribution of different corners to different plasmonic modes remains unknown especially for tilted decahedra with one face in contact with the substrate. Employing site specific spectroscopy using CL-SEM, we recorded spectra at different symmetry points of the same particle. This process allows us to detect a quadrupolar resonance at one corner of the decahedra whereas excitations at the other corners are dominated by dipolar resonance. The spatial features of dipole and quadrupolar modes imaged using CL-SEM (Figure 2b–h) from decahedra has not been reported so far to the best of our knowledge.

Recently, an elegant comparative study<sup>25</sup> among the three techniques, namely, DFM, EELS, and CL imaging spectroscopy in a SEM, for the plasmonic characterization of a single Au decahedron of side edge length  $\sim 58$  nm revealed that the azimuthal and the polar dipole mode could be accessed through EELS to get high resolution spectral and spatial domain information whereas the CL provided the information on spectral signature of the azimuthal dipolar mode only. However, due to the larger decahedra used (edge length 110 nm) in our present study the retardation effect comes into play to access a quadrupolar mode ( $M_2$ ) for excitation at corner 2 (Figure 1). The BEM simulated CL studies by Myroshnychenko et al.<sup>25</sup> predicted the azimuthal dipole mode for the vertically standing 58 nm Au decahedron to be peaked at 2.25 eV, whereas the same mode appeared in the present FDTD simulated CL studies for our vertically standing 110 nm Au decahedron on Si at 2.03 eV (610 nm) (see spectrum for  $\theta = 0^\circ$  shown in Figure 3). The red shift of the azimuthal mode in the present case with respect to that of Myroshnychenko et al.<sup>25</sup> arises due to the combined effect of a larger particle size and the presence of a high index substrate. The ratio of the maximum intensity of the polar mode to that of the azimuthal mode amounts roughly to 1/3 in our experimental and simulated CL spectra obtained for a tilted decahedron geometry, which is slightly different from the reported value of 1/4 in ref 25. In the EELS studies by Myroshnychenko et al.<sup>25</sup> for the Au decahedron of edge length  $\sim 65$  nm sitting on a mica substrate two distinct dipole plasmon modes emerged, one of them being dominant in the two corners in contact with the substrate and the other one being stronger in the other three corners. In the present CL experiment of Au decahedron sitting on high index substrate Si, it is difficult to get a detectable luminescence from the corners in contact with the substrate as most of the emission will go toward the higher index substrate and will not reach the detector hindering us the direct comparison between CL and EELS results for the e-beam excitation at corners 4 and 5 of our sample.

The current study demonstrates several new aspects that have not been reported before for the decahedral nanoparticle to the best of the authors' knowledge. First, employing a simple direct emission imaging technique such as CL-SEM, we imaged the plasmonic modes of a single Au decahedron with high spatial resolution. Second, we confirm the presence of two dipolar and one quadrupolar mode when the decahedron is



probed at different locations with the e-beam. Finally, we presented a direct simulation of the CL spectra and 2D-CL image that mimics the actual CL experiment. As an electron microscopy tool for probing LSP, CL-SEM can act as a complementary tool to EELS, and in the domain of thick structures where EELS cannot be applied, it is the only electron microscopy based technique to probe plasmons with unmatched spatial resolution.

## CONCLUSIONS

In conclusion, we have performed site specific CL spectroscopy and imaging in a field emission gun scanning electron microscope to study plasmonic response of isolated gold decahedra of side edge length  $\sim 110$  nm and tilted by an angle  $40^\circ$  supported on a silicon substrate. Our experiment demonstrates that such an asymmetric structure gives rise to a strong electric field confinement at different corners as well as the apex which has been recorded in spectral and spatial domain using CL spectroscopy and imaging for the first time. Comparing the experimental spectra and near-field maps with the spectra, intensity maps and the vector plots of the electric field obtained from the FDTD simulation, we identified two dipole-active plasmon modes along the azimuthal and polar direction in addition to a quadrupole mode of the decahedral gold nanoparticle. The present study clearly indicates that CL spectroscopy and imaging performed in a field emission gun SEM can be regarded as a true single particle spectroscopy technique and can be considered as a good complementary tool to EELS in the area of plasmonic research. The theoretical approach and experimental methodology presented here could be used to investigate a wide range of nanoparticle geometries and associated surface plasmon modes, thus giving insight into the light matter interaction at nanometer scale and may help improve the design of new plasmonic devices.

## ASSOCIATED CONTENT

### Supporting Information

Effect of dispersive and non dispersive substrate on the simulated spectra (Figure SI.1). This material is available free of charge via the Internet at <http://pubs.acs.org>.

## AUTHOR INFORMATION

### Corresponding Author

\*E-mail: [tapask.chini@saha.ac.in](mailto:tapask.chini@saha.ac.in). Fax: +91 33 2337 4637.

### Notes

The authors declare no competing financial interest.

## ACKNOWLEDGMENTS

The authors thank Dr. James Pond of Lumerical Solutions Inc. for technical assistance and critical reading of the manuscript. We are also grateful to the anonymous referees for the constructive criticisms of our paper.

## REFERENCES

- (1) Maier, S. A. *Plasmonics: Fundamentals and Applications*; Springer: New York, 2007.
- (2) Stockman, M. I. *Opt. Express* **2011**, *19*, 22029–22106.
- (3) García de Abajo, F. J. *Rev. Mod. Phys.* **2010**, *82*, 209–275.
- (4) Wang, Y. K.; Yang, T. Y.; Tuominen, M. T.; Achermann, M. *Phys. Rev. Lett.* **2009**, *102*, 163001 (1–4).
- (5) Atwater, H. A.; Polman, A. *Nat. Mater.* **2010**, *9*, 205–213.

- (6) Alonso-González, P.; Albella, P.; Schnell, M.; Chen, J.; Huth, F.; García-Etxarri, A.; Casanova, F.; Golmar, F.; Arzubiaga, L.; Hueso, L. E.; Aizpurua, J.; Hillenbrand, R. *Nat. Commun.* **2012**, *3*, 684 (1–7).
- (7) Myroshnychenko, V.; Rodríguez-Fernández, J.; Pastoriza-Santos, I.; Funston, A. M.; Novo, C.; Mulvaney, P.; Liz-Marzán, L. M.; García de Abajo, F. J. *Chem. Soc. Rev.* **2008**, *37*, 1792–1805.
- (8) Song, Y.; Zhang, Z.; Elsayed-Ali, H. E.; Wang, H.; Henry, L. L.; Wang, Q.; Zoud, S.; Zhang, T. *Nanoscale* **2011**, *3*, 31–44.
- (9) Scholl, J. A.; Koh, A. L.; Dionne, J. A. *Nature* **2012**, *483*, 421–428.
- (10) Duan, H.; Fernández-Domínguez, A. I.; Bosman, M.; Maier, S. A.; Yang, J. K. W. *Nano Lett.* **2012**, *12*, 1683–1689.
- (11) Yamamoto, N.; Araya, K.; García de Abajo, F. J. *Phys. Rev. B* **2001**, *64*, 205419(1–9).
- (12) Vesseur, E. J. R.; de Waele, R.; Kuttge, M.; Polman, A. *Nano Lett.* **2007**, *7*, 2843–2846.
- (13) Vesseur, E. J. R.; de Waele, R.; Lezec, H. J.; Atwater, H. A.; García de Abajo, F. J.; Polman, A. *Appl. Phys. Lett.* **2008**, *92*, 083110 (1–3).
- (14) Rang, M.; Jones, A. C.; Zhou, F.; Li, Z. Y.; Wiley, B. J.; Xia, Y.; Raschke, M. B. *Nano Lett.* **2008**, *8*, 3357–3363.
- (15) Chaturvedi, P.; Hsu, K. H.; Kumar, A.; Fung, K. H.; Mabon, J. C.; Fang, N. X. *ACS Nano* **2009**, *3*, 2965–2974.
- (16) Das, P.; Chini, T. K.; Pond, J. J. *Phys. Chem. C* **2012**, *116*, 15610–15619.
- (17) Sönnichsen, C.; Franzl, T.; Wilk, T.; von Plessen, G.; Feldmann, J.; Wilson, O.; Mulvaney, P. *Phys. Rev. Lett.* **2002**, *88*, 077402 (1–4).
- (18) Song, Y.; Nallathamby, P. D.; Huang, T.; Elsayed-Ali, H. E.; Xu, X.-H. Nancy. *J. Phys. Chem. C* **2010**, *114*, 74–81.
- (19) Henry, A. I.; Bingham, J. M.; Ringe, E.; Marks, L. D.; Schatz, G. C.; Van Duyne, R. P. *J. Phys. Chem. C* **2011**, *115*, 9291–9305.
- (20) Rodríguez-Fernández, J.; Novo, C.; Myroshnychenko, V.; Funston, A. M.; Sánchez-Iglesias, A.; Pastoriza-Santos, I.; Pérez-Juste, J.; García de Abajo, F. J.; Liz-Marzán, L. M.; Mulvaney, P. *J. Phys. Chem. C* **2009**, *113*, 18623–18631.
- (21) Pastoriza-Santos, I.; Sánchez-Iglesias, A.; F. García de Abajo, F. J.; Liz-Marzán, L. M. *Adv. Funct. Mater.* **2007**, *17*, 1443–1450.
- (22) Vesseur, E. J. R. *Electron beam imaging and spectroscopy of plasmonic nanoantenna resonances*. Ph.D. Thesis, Utrecht University, 2011.
- (23) Nelayah, J.; Kociak, M.; Stéphan, O.; García de Abajo, F. J.; Tencé, M.; Henrard, L.; Taverna, D.; Pastoriza-Santos, I.; Liz-Marzán, L. M.; Colliex, C. *Nat. Phys.* **2007**, *3*, 348–353.
- (24) Gu, L.; Sigle, W.; Koch, C. T.; Ögüt, B.; van Aken, P. A.; Talebi, N.; Vogelgesang, R.; Mu, J.; Wen, X.; Mao, J. *Phys. Rev. B* **2011**, *83*, 195433 (1–7).
- (25) Myroshnychenko, V.; Nelayah, J.; Adamo, G.; Geuquet, N.; Rodríguez-Fernández, J.; Pastoriza-Santos, I.; MacDonald, K. F.; Henrard, L.; Liz-Marzán, L. M.; Zheludev, N. I.; Kociak, M.; García de Abajo, F. J. *Nano Lett.* **2012**, *12*, 4172–4180.
- (26) Sánchez-Iglesias, A.; Pastoriza-Santos, I.; Pérez-Juste, J.; Rodríguez-González, B.; García de Abajo, F. J.; Liz-Marzán, L. M. *Adv. Mater.* **2006**, *18*, 2529–2534.
- (27) Liu, M.; Guyot-Sionnest, P.; Lee, T. W.; Gray, S. K. *Phys. Rev. B* **2007**, *76*, 235428 (1–10).
- (28) Liu, M.; Lee, T. W.; Gray, S. K.; Guyot-Sionnest, P.; Pelton, M. *Phys. Rev. Lett.* **2009**, *102*, 107401 (1–4).
- (29) García de Abajo, F. J.; Kociak, M. *Phys. Rev. Lett.* **2008**, *100*, 106804 (1–4).
- (30) Kuttge, M.; Vesseur, E. J. R.; Koenderink, A. F.; Lezec, H. J.; Atwater, H. A.; García de Abajo, F. J.; Polman, A. *Phys. Rev. B* **2009**, *79*, 113405(1–4).
- (31) Sapienza, R.; Coenen, T.; Renger, J.; Kuttge, M.; van Hulst, N. F.; Polman, A. *Nat. Mat.* **2012**, *11*, 781–787.
- (32) Wu, H. Y.; Chu, H. C.; Kuo, T. J.; Kuo, C. L.; Huang, M. L. *Chem. Mater.* **2005**, *17*, 6447–6451.
- (33) Das, P.; Chini, T. K. *Curr. Sci.* **2011**, *101*, 849–854.
- (34) Lide, D. R. *CRC Handbook of Chemistry and Physics*, 86th ed.; Taylor and Francis: London, UK, 2005.



- (35) Soller, B. J.; Stuart, H. R.; Hall, D. G. *Opt. Lett.* **2001**, *26*, 1421–1423.
- (36) Sherry, L. J.; Chang, S. H.; Schatz, G. C.; Van Duyne, R. P. *Nano Lett.* **2005**, *5*, 2034–2038.
- (37) Ringe, E.; McMahon, J. M.; Sohn, K.; Cobley, C.; Xia, Y.; Huang, J.; Schatz, G. C.; Marks, L. D.; Van Duyne, R. P. *J. Phys. Chem. C* **2010**, *114*, 12511–12516.
- (38) Mazzucco, S.; Geuquet, N.; Ye, J.; Stéphan, O.; Van Roy, W.; Van Dorpe, P.; Henrard, L.; Kociak, M. *Nano Lett.* **2012**, *12*, 1288–1294.